GOES Climatology and Analysis of Thunderstorms with Enhanced 3.9-μm Reflectivity

DANIEL T. LINDSEY AND DONALD W. HILLGER

NOAA/NESDIS/ORA/RAMMB, Fort Collins, Colorado

LOUIE GRASSO, JOHN A. KNAFF, AND JOHN F. DOSTALEK

Cooperative Institute for Research in the Atmosphere, Fort Collins, Colorado

(Manuscript received 31 October 2005, in final form 10 January 2006)

ABSTRACT

By combining observations from the Geostationary Operational Environmental Satellite (GOES) 3.9- and 10.7-μm channels, the reflected component of the 3.9-μm radiance can be isolated. In this paper, these 3.9-μm reflectivity measurements of thunderstorm tops are studied in terms of their climatological values and their utility in diagnosing cloud-top microphysical structure. These measurements provide information about internal thunderstorm processes, including updraft strength, and may be useful for severe weather nowcasting. Three years of summertime thunderstorm-top 3.9-μm reflectivity values are analyzed to produce maps of climatological means across the United States. Maxima occur in the high plains and Rocky Mountain regions, while lower values are observed over much of the eastern United States. A simple model is used to establish a relationship between 3.9-μm reflectivity and ice crystal size at cloud top. As the mean diameter of a cloud-top ice crystal distribution decreases, more solar radiation near 3.9 μm is reflected. Using the North American Regional Reanalysis dataset, the thermodynamic environment that favors thunderstorms with large 3.9-μm reflectivity values is identified. In the high plains and mountains, environments with relatively dry boundary layers, steep lapse rates, and large vertical shear values favor thunderstorms with enhanced 3.9-μm reflectivity. Thunderstorm processes that lead to small ice crystals at cloud top are discussed, and a possible relationship between updraft strength and 3.9-μm reflectivity is presented.

1. Introduction

Satellite observations of thunderstorms have been widely documented since the launch of Geostationary Operational Environmental Satellites (GOES) in the 1970s. The Visible and Infrared Spin Scan Radiometer (VISSR) Atmospheric Sounder (VAS), aboard *GOES-4* (launched in 1980) was the first instrument to detect radiation in the shortwave window, that portion of the electromagnetic spectrum between 3.5 and 4.0 μm (Kidder and Vonder Haar 1995). More recent GOES imagers, beginning with *GOES-8*, have a channel centered near 3.9 μm. At night, differences in 3.9- and 10.7-μm radiance provide information about cloud-top microphysics (Ellrod 1995). During the daytime, radiances at this wavelength include both an emitted earth–atmosphere component and a reflected solar component. For clouds of sufficient optical thickness, the thermal component at 3.9 μm can be approximated by assuming the emitting temperature at 10.7 μm is the same at 3.9 μm (Setvák and Doswell 1991). Given the observed 3.9- and 10.7-μm radiances, it is then possible to calculate the 3.9-μm solar reflected component. This is often represented as the percent of incoming solar radiation at 3.9 μm that is reflected back to the satellite (e.g., Allen et al. 1990; Kidder et al. 2000), and will hereafter be referred to as the 3.9-μm reflectivity.

Thunderstorm tops with enhanced reflectivity at 3.7 μm were first noted using Advanced Very High Resolution Radiometer (AVHRR) data (e.g., Liljas 1987; Scorer 1987). Setvák and Doswell (1991) suggested that differences in 3.7-μm reflectivity may be due to differences in microphysical structure at cloud top. It is well documented that liquid water clouds are more effective reflectors of 3.5–4.0-μm radiation than ice water clouds

Corresponding author address: Daniel T. Lindsey, CIRA/Colorado State University, 1375 Campus Delivery, Fort Collins, CO 80523-1375.
E-mail: lindsey@cira.colostate.edu

(e.g., Turk et al. 1998). However, the majority of thunderstorm tops exist at temperatures well below −40°C, meaning their composition is dominated by ice crystals. Differences in the size distributions of these ice crystals have an effect on 3.5–4.0-μm reflectivity. Past studies have shown that more numerous smaller crystals tend to be more effective reflectors at 3.7 μm (Melani et al. 2003a,b). In addition, Setvák et al. (2003) observed similar thunderstorm-top reflectivity characteristics at 3.9 μm from GOES as at 3.7 μm from AVHRR. The most likely hypothesis is that the detection of a thunderstorm top with enhanced 3.9-μm reflectivity implies that its anvil is composed of relatively small and numerous ice crystals, and this may provide information about internal thunderstorm structure (Setvák et al. 2003).

Examples of thunderstorms with relatively high and low 3.9-μm reflectivities are given in Figs. 1a and 1b, respectively. Values of 3.9-μm reflectivity for storms on the plains in Fig. 1a approach 15% (warmer colors), while values for most of the storms in Fig. 1b are less than 5% (cooler colors).

The primary goals of this study are to examine the 3.9-μm reflectivity of thunderstorms from a climatological perspective, seek mechanisms for the existence of small ice crystals at cloud top, and find possible explanations for variations in cloud-top 3.9-μm reflectivity between storms. The analysis reveals a connection between 3.9-μm reflectivity and thunderstorm updraft strength, providing an extremely useful severe weather nowcasting application. Section 2 describes a climatological study of thunderstorm-top 3.9-μm reflectivity over the United States, section 3 describes modeling results linking ice crystal size to 3.9-μm reflectivity, section 4 presents the results of a statistical study using reanalysis data, section 5 presents a possible physical mechanism, and section 6 offers some concluding remarks.

2. Thunderstorm 3.9-μm reflectivity climatology

Values of 3.9-μm reflectivity are calculated from GOES radiance observations using the method described by Setvák and Doswell (1991). The GOES radiance at 3.9 μm can be split into two components:

$$R_{3.9} = R_{r_{3.9}} + \varepsilon_{3.9} R_{e_{3.9}}(T), \tag{1}$$

where $R_{3.9}$ is the total radiance at the band centered at 3.9 μm, $R_{r_{3.9}}$ is the solar-reflected component at 3.9 μm, $\varepsilon_{3.9}$ is the emissivity of the scene at 3.9 μm, and $R_{e_{3.9}}(T)$ is the blackbody radiance 3.9 μm with temperature T. The first term can be written as

$$R_{r_{3.9}} = \alpha_{3.9}\left[R_{e_{3.9}}(T_{\text{sun}})\left(\frac{A}{B}\right)^2 \cos(\phi) \right], \tag{2}$$

where $\alpha_{3.9}$ is the 3.9-μm reflectivity, $R_{e_{3.9}}(T_{\text{sun}})$ is the blackbody radiance of the sun (T_{sun} is taken to be 5800 K), A is the radius of the sun, B is the average radius of earth's orbit, and ϕ is the solar zenith angle. For simplicity, the quantity in brackets will be denoted S, or the solar flux at the top of the atmosphere. For a cloud of sufficient optical thickness, the transmissivity is approximately zero. This approximation, along with Kirchoff's law, gives

$$\varepsilon_{3.9} + \alpha_{3.9} = 1. \tag{3}$$

Substituting Eqs. (2) and (3) into Eq. (1), the 3.9-μm reflectivity is given by

$$\alpha_{3.9} = \frac{R_{3.9} - R_{e_{3.9}}(T)}{S - R_{e_{3.9}}(T)}. \tag{4}$$

To calculate this quantity, we estimate the 3.9-μm blackbody emitting temperature by using the observed 10.7-μm brightness temperature. This requires that the emissivity at 10.7 μm be unity, which for an optically thick cloud is a reasonable approximation (Stephens 1978). Finally, it is assumed that the reflected radiation is isotropic.

Data from GOES-West, currently *GOES-10* and centered at 135°W, and GOES-East, currently *GOES-12* and centered at 75°W, were analyzed every 2 h during May, June, July, and August of 2000, 2003, and 2004. Using Eq. (4), the 3.9-μm reflectivity values were calculated at every ice cloud pixel within the domain for every month within the chosen period. For the purposes of this study, we define an ice cloud pixel as one in which the 10.7-μm brightness temperature is colder than −40°C. This restriction eliminates thin cirrus, minimizes transmission from below, and ensures that all cloud tops are composed almost entirely of ice crystals. Since the analysis is limited to summer months, we assume that these ice cloud pixels are associated with convectively generated clouds. Equations (2) and (4) show that the 3.9-μm reflectivity calculation becomes undefined as the solar zenith angle approaches 90°, so only those pixels with a solar zenith angle of less than 68° were included. This value was chosen by producing a scatterplot of observed 3.9-μm reflectivity versus solar zenith angle for a large number of pixels, and noting that all reflectivities begin to increase as the zenith angle exceeds 68°. During summer month afternoons, the sun typically reaches 68° between 1800 and 1900 local daylight time, so evening and overnight convection is excluded from this analysis.

Figure 2a shows the results of the GOES-East clima-

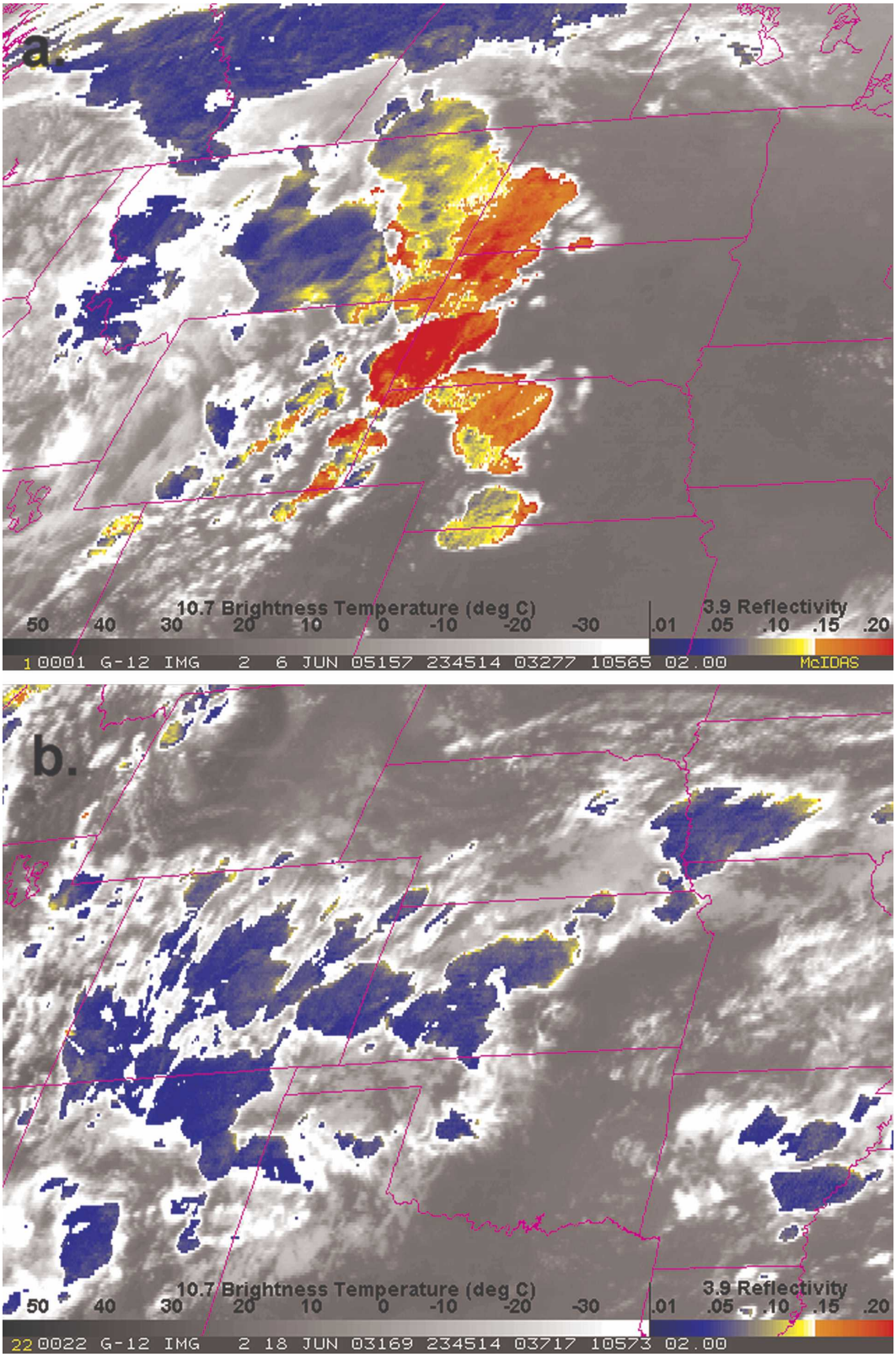

FIG. 1. *GOES-12* 3.9-μm reflectivity for brightness temperatures less than -40°C (in colors), and 10.7 μm (gray shades) for brightness temperatures greater than -40°C for (a) 2345 UTC 6 Jun 2005 and (b) 2315 UTC 18 Jun 2003. Warmer colors indicate cold cloud tops with larger 3.9-μm reflectivity values.

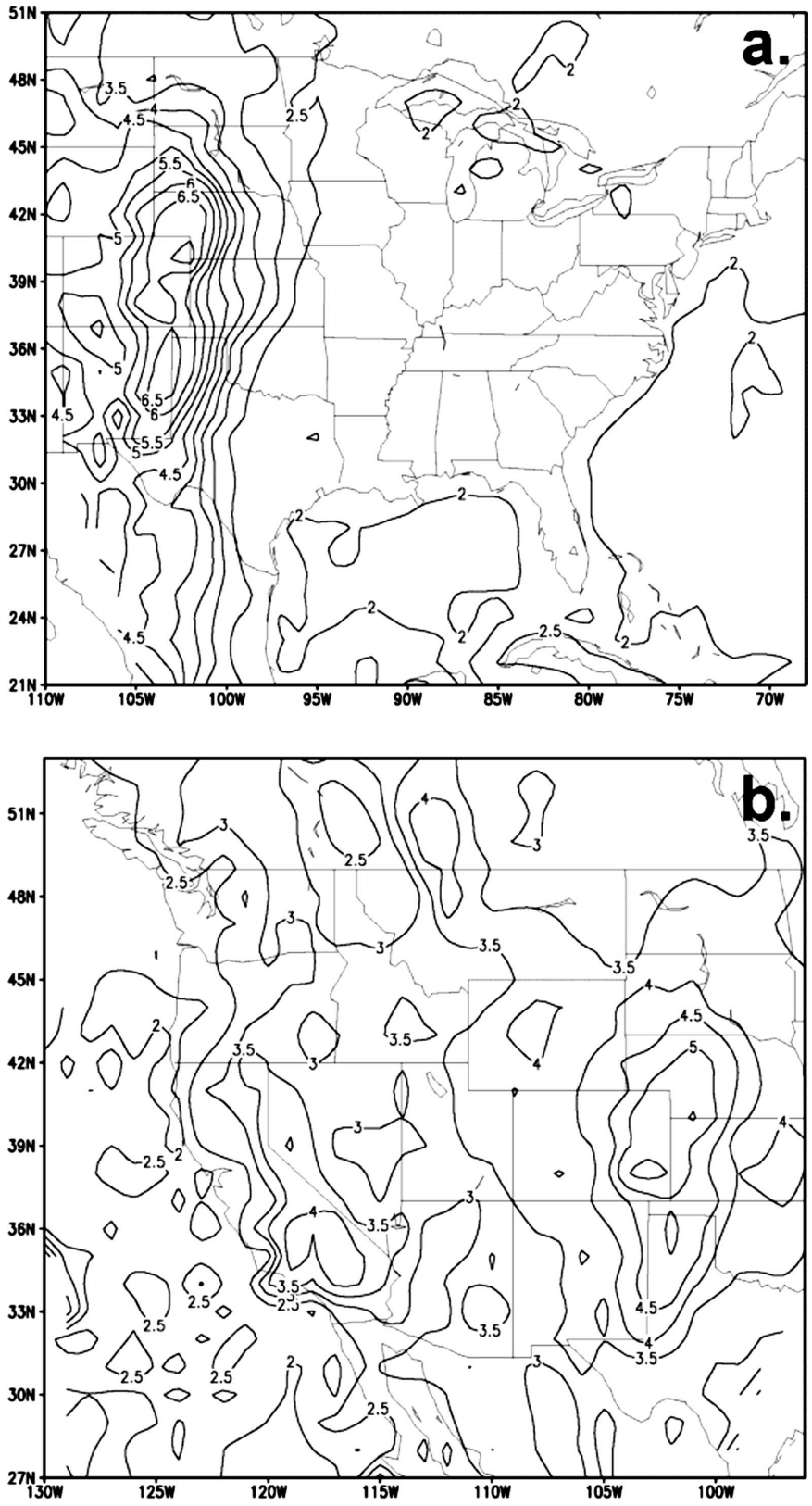

FIG. 2. Mean 3.9-μm reflectivities of ice clouds from (a) GOES-East and (b) GOES-West, during May, June, July, and August of 2000, 2003, and 2004, when the solar zenith angle is less than 68°.

TABLE 1. Mean 3.9-μm reflectivities from GOES-East (G-E) and GOES-West (G-W) for different times and reflection angles from 26 Jun 2004.

Time (UTC)	G-E reflection angle (°)	G-W reflection angle (°)	G-E 3.9 μm mean reflectivities (std dev)	G-W 3.9 μm mean reflectivities (std dev)
2345	105	46	7.30 (2.37)	4.00 (1.56)
2315	99	41	5.86 (2.19)	3.98 (1.75)
2245	92	36	4.57 (1.80)	3.75 (1.83)
2215	85	32	3.89 (1.64)	3.73 (2.02)
2045	65	30	2.58 (1.02)	3.05 (1.63)
2015	59	33	2.50 (0.96)	2.92 (1.49)
1945	52	37	2.13 (0.87)	2.38 (1.28)
1915	46	42	2.23 (1.11)	2.20 (1.14)
1845	41	47	2.13 (1.23)	2.05 (1.09)
1745	32	60	1.66 (0.91)	1.70 (0.60)
1715	29	66	1.88 (0.25)	2.08 (0.41)
1645	29	73	1.87 (0.24)	2.34 (0.21)
1615	30	80	1.91 (0.26)	2.41 (0.22)

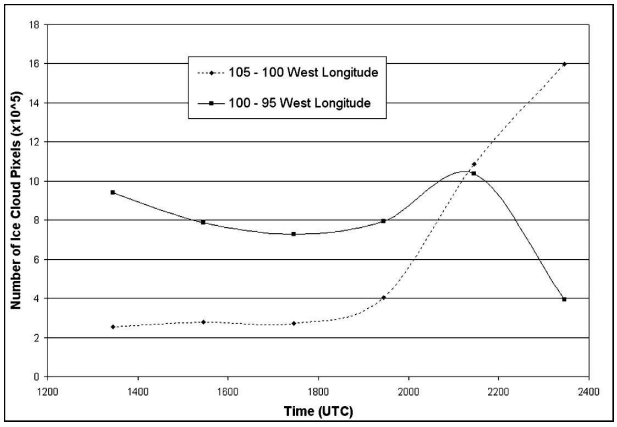

FIG. 3. Diurnal trend in ice cloud pixels used in the analysis from Fig. 2, for the longitudinal bands 105°–100°W and 100°–95°W, from GOES-East.

tology. Infrared pixels were grouped into 1° × 1° latitude–longitude boxes before calculating the mean reflectivity values; detail would be lost with the use of larger boxes, and the use of smaller boxes would introduce noise. All boxes over the United States contain at least 10^4 total pixels. Contours in Fig. 2 represent the mean 3.9-μm reflectivity of ice clouds. Over much of the eastern United States, values are near 2%, while in the high plains and the Rocky Mountain region, reflectivities are greater than 5%. The GOES-West climatology (Fig. 2b) shows generally larger values than in the eastern United States, with maxima occurring in eastern Colorado, northwestern Montana, and eastern California. The longitudinal band between 110°–95°W was viewed by both satellites, and GOES-East values are generally about 1% larger. Conversely, in the longitudinal band between 100° and 95°W, GOES-West values are about 1% larger. The result is a larger east–west gradient in mean reflectivity as viewed from GOES-East compared with GOES-West.

To investigate this difference between GOES-East and GOES-West 3.9-μm reflectivities, a day was chosen that had ice clouds in the longitudinal band covered by both satellites in both the morning and afternoon (26 June 2004). Ice cloud pixels viewed by both satellites at approximately the same time were selected, and their 3.9-μm reflectivities were calculated. Table 1 shows the means and standard deviations for various times throughout the day, and the associated reflection angles between the sun and satellite for each pixel. The reflection angles varied slightly with location at a given time, so the mean angles are displayed in the table. Note that in the late afternoon (2345 UTC), 3.9-μm reflectivities are maximized, and GOES-East measures over 3% greater values than GOES-West. At this time, the GOES-East reflection angle is 105° compared to 46° with GOES-West. GOES-East is therefore in a position to measure more forward-scattered radiation than GOES-West, so forward scattering appears to be favored. Earlier in the day, as the reflection angles become closer together, the differences in 3.9-μm reflectivities also decrease. In the morning, reflectivities measured from GOES-West exceed those from GOES-East, but due to a lack of vigorous convection, the absolute values are quite low. This analysis suggests that forward scattering is always preferred, and is maximized for large reflection angles.

Figure 3 shows the diurnal trend in ice cloud pixel frequency for two longitudinal bands. In the morning, ice clouds are much more frequent in the eastern band. These clouds are likely associated with the remnants of nocturnal convective systems that often exist in the central plains shortly after sunrise. The western band shows a distinct afternoon maximum in convective ice clouds. The apparent dropoff in ice cloud frequency in the eastern band at 2345 UTC is primarily an artifact of the 68° zenith angle requirement; many areas in this band have zenith angles greater than 68° at 2345 UTC, so those pixels are not included in the analysis, as explained above. Results from Table 1 combined with Fig. 3 explain the differences in 3.9-μm reflectivities as measured from GOES-East and GOES-West. Since forward scattering is preferred, and GOES-East is in a position to measure more forward-scattered radiation during the peak in ice cloud frequency in late afternoon, mean values are higher from GOES-East in the longitudinal band between 105° and 100°W. In the eastern band, morning ice clouds are quite frequent, during which

time GOES-West measures more forward-scattered radiation, making these mean values slightly larger than those from GOES-West. These results are consistent with similar findings by Setvák et al. (2003) and show that the scattering is not isotropic. Future work will involve correcting for preferential scattering when calculating 3.9-μm reflectivity.

Figures 4a and 4b show the same data as Fig. 2 from a slightly different perspective. Here, the percent of ice cloud pixels whose 3.9-μm reflectivity is greater than 5% is contoured. The choice of the 5% threshold was arbitrary; changing the threshold had a negligible effect on the resulting geographical distribution. In Fig. 4a, note that in the high plains over 50% of ice clouds have greater than 5% 3.9-μm reflectivity, while farther east, less than 10% exceed this threshold. This, along with a more thorough analysis of distributions about the mean, show that reflectivities greater than 5% are rare in the east. In the longitudinal band between 110° and 100°W, values greater than 5% are quite common, and reflectivities greater than 10% are not infrequent. In both Figs. 2 and 4, maxima occur at or near major mountain ranges, suggesting that high terrain may play a role in the physical mechanism responsible for thunderstorms with "enhanced" 3.9-μm reflectivity, defined here to be greater than 5%. This will be investigated further and discussed in sections 4 and 5. It should also be noted that mountain wave clouds tend to have relatively large 3.9-μm reflectivities and could, therefore, be contributing to the larger means near mountain ranges. However, during the summer months, convectively generated ice clouds are far more common than mountain wave clouds, so we assume the mean is dominated by thunderstorm reflectivity.

3. Relationship between ice crystal size and 3.9-μm reflectivity

In this section, we examine the sensitivity of 3.9-μm reflectivity to ice crystal size at cloud top. Grasso and Greenwald (2004) successfully generated synthetic GOES brightness temperatures associated with simulated mesoscale weather events. The methods used relied on two models: a cloud-resolving model and an observational operator. The cloud-resolving model was used to simulate a thunderstorm event, and its output was then used as input to the observational operator. This tool first computes gaseous transmittance at a specific wavelength. Next, mass mixing ratio and number concentration of each of the seven hydrometeor types from the cloud model are used to compute three bulk optical properties of the simulated cloud: extinction, single scatter albedo, and asymmetry factor. These optical properties are then used by radiative transfer models to compute brightness temperatures at a specified wavelength (for more details, see Greenwald et al. 2002).

Instead of running a complicated cloud-resolving model, a simpler approach was adopted, where an idealized cloud composed of planar polycrystals (Mitchell 1996) was specified in the layer between 10 and 12 km AGL. Using a gamma size distribution (Mitchell 2000), the mean ice crystal diameter can be controlled by varying the mass mixing ratio and number concentration of ice crystals. For each mean diameter, the observational operator was used to calculate synthetic GOES radiance values. From the radiances, the 3.9-μm reflectivity was computed and plotted as a function of mean diameter, for three different solar zenith angles (Fig. 5). In all of these cases, the top of the ice cloud was located near the tropopause, at a temperature near −53°C.

For a given solar zenith angle, the 3.9-μm reflectivity is fairly insensitive to ice crystal size for diameters greater than about 80 μm, but for smaller diameters the 3.9-μm reflectivity increases more rapidly. According to the model, increasing the solar zenith angle also produces an increase in 3.9-μm reflectivity for a given ice crystal size. The important result is that 3.9-μm reflectivity increases dramatically for small ice crystal sizes. While 3.9-μm reflectivity shows great variability, the simulated 10.7-μm brightness temperatures are near −53°C (approximately the tropopause temperature in the model) for all ice crystal sizes. This result implies that the cloud was of sufficient optical thickness to prevent any emitted terrestrial radiation from penetrating the cloud layer.

Observational confirmation of these results is fairly difficult with current techniques. A direct comparison of aircraft-measured ice crystal sizes and satellite-measured 3.9-μm reflectivity is difficult for several reasons. First, reflection of radiation by an optically thick cirrus cloud is achieved by a population of ice crystals that exists over at least tens of meters in the vertical, so aircraft sampling at a single altitude may be unrepresentative of the mean size distribution of the reflecting layer. Second, the 4-km satellite resolution is rather coarse, so many aircraft legs through a single satellite pixel would be required to estimate the satellite-observed mean ice crystal size. Despite these limitations, a recent study from the 2002 Cirrus Regional Study of Tropical Anvils and Cirrus Layers-Florida Area Cirrus Experiment (CRYSTAL-FACE), in which anvils of convective clouds were sampled by aircraft to collect and measure ice crystals, is quite relevant to this study and will be discussed in section 5.

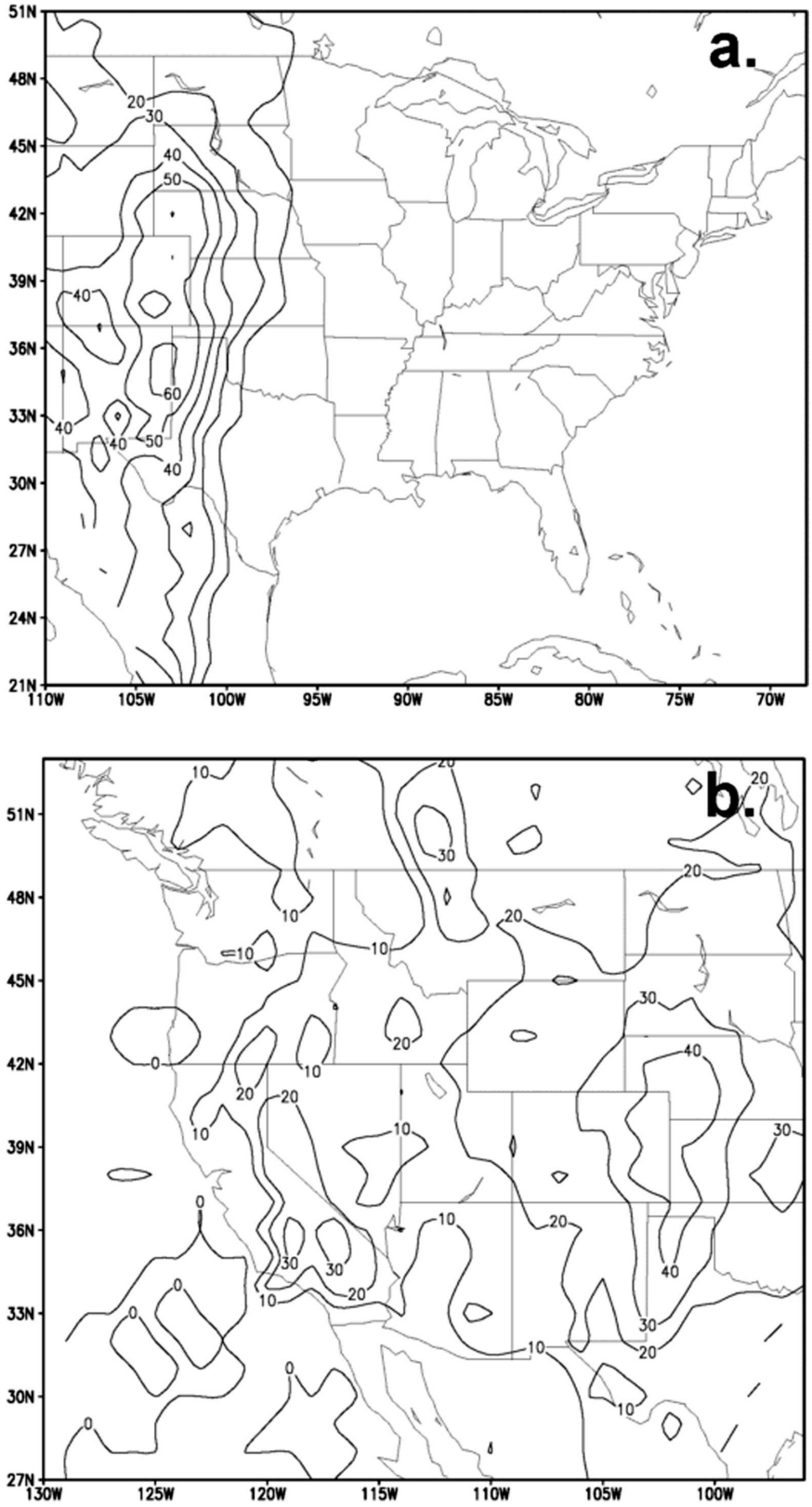

FIG. 4. Percent of ice clouds whose 3.9-μm reflectivity exceeds 5% from (a) GOES-East and (b) GOES-West, during May, June, July, and August of 2000, 2003, and 2004, for times when the solar zenith angle is less than 68°.

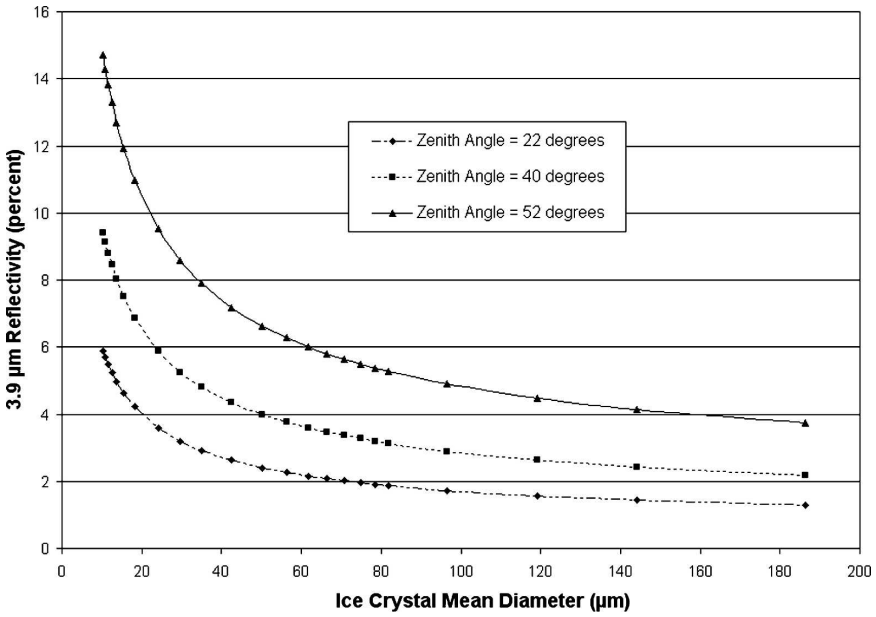

FIG. 5. Model results for 2-km-thick cloud composed of ice crystals, for three solar zenith angles.

4. Statistical analysis of thermodynamic environment

To investigate whether thermodynamics play a role in producing thunderstorms with enhanced 3.9-μm reflectivity, a composite analysis was performed over the high plains region having the largest mean cloud reflectivity values (Fig. 2a). The analysis domain was chosen roughly within the 4.5% contour in Fig. 2a, or between approximately 30°–45°N and between 100°–110°W. GOES data during the summer months (June, July, August) of 2003 and 2004 were analyzed, and 16 convective days having a large percentage of thunderstorm tops with 3.9-μm reflectivities greater than 5% (hereafter referred to as "reflective days") and 16 convective days having a low percentage of thunderstorm tops with 3.9-μm reflectivities greater than 5% ("nonreflective days") were selected. Days similar to those in Figs. 1a and 1b are typical examples of a reflective day and a nonreflective day, respectively.

For each of the 16 reflective and 16 nonreflective days, a subset of the domain was chosen based on the location of convective activity. Within this smaller area, all grid points from the North American Regional Reanalysis (NARR) dataset (Mesinger et al. 2006) were extracted. This dataset uses the National Centers for Environmental Prediction (NCEP) Eta Model and its data assimilation system, so its horizontal grid spacing is 32 km, it contains 45 vertical levels, and output is available every 3 h. Additionally, observed precipitation is assimilated hourly and other datasets are incorporated, such as the Noah land surface model. For more details about the NARR, see Mesinger et al. (2006). For each of the 32 days in the analysis, between 500 and 1000 grid points were selected within the subset having convective activity. The 0000 UTC values of temperature, dewpoint, and wind for the entire troposphere were averaged for each of the 16 days. These mean profiles were then averaged for the reflective days and nonreflective days, producing two final mean profiles (Fig. 6). Many of the grid points used in this analysis have surface pressures below 850 hPa, so the profiles are most meaningful at pressures below 850 hPa.

There are several important differences between these two mean profiles. First, the relative humidity throughout the reflective profile is lower, especially in the lowest 400 hPa. A larger dewpoint depression near the surface suggests that a fairly dry boundary layer is supportive of thunderstorm tops with enhanced 3.9-μm reflectivity. Second, and possibly more importantly, the 800–300-hPa lapse rate is noticeably steeper in the reflective case. This more unstable environment would promote stronger updrafts. Finally, the midlevel westerlies are stronger in the reflective case, resulting in larger surface–500-hPa shear.

To get a more quantitative understanding of the results, values of selected variables were collected at each grid point, and means and standard deviations were calculated for each of the 32 days. Next, the resulting

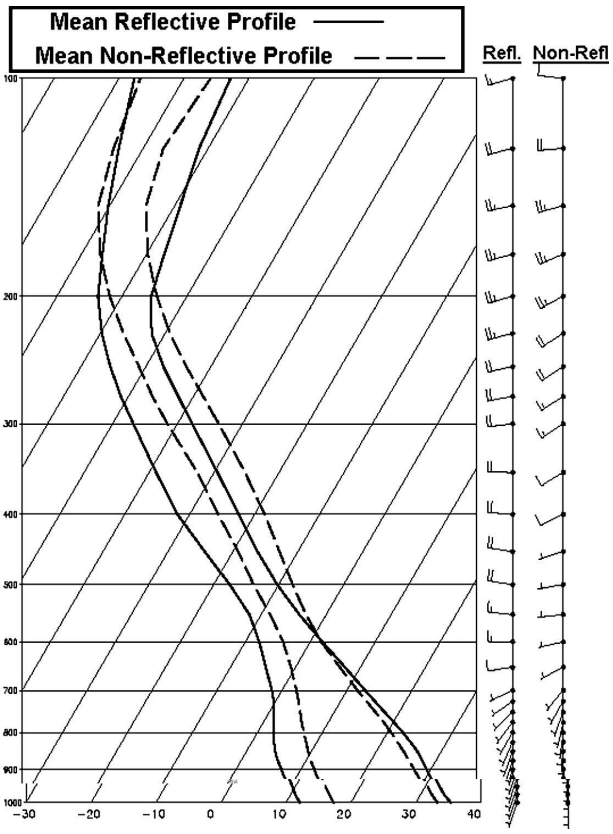

FIG. 6. Mean (right) temperature and (left) dewpoint profiles for the reflective (solid) and nonreflective (dashed) cases, along with mean wind profiles, plotted on a traditional skew T–log$p$ diagram. A full wind barb represents 10 kt.

means were averaged together for each case (reflective and nonreflective), and the standard deviations were also averaged. Results are given in Table 2. To estimate significance, a difference-of-means t test was performed using the mean standard deviations calculated above. Values in Table 2 with greater than 95% significance are set in italics; those exceeding 99% significance are set in bold.

The convective available potential energy (CAPE) for the reflective case is over twice that of the nonreflective case, verifying that instability is greater in the reflective situation (even though convection was observed in both cases). Precipitable water values are smaller and 700-hPa relative humidity values are lower for the reflective case, further underscoring the possible importance of relatively dry air. Lapse rates are significantly steeper in the reflective case (the standard deviations for lapse rate were very small), and the surface–500-hPa zonal shear is much larger on reflective days. Surface temperature and dewpoint values were used to calculate the lifted condensation level (LCL). Using this as the cloud-base height, the distance from

TABLE 2. Means for several parameters for the 16 reflective days and 16 nonreflective days. Italicized numbers indicate the difference of means exceeds 95% significance; boldface numbers show the difference of means exceeding 99% significance.

Parameter	Reflective case mean	Nonreflective case mean
CAPE (J kg^{-1})	*567*	*219*
Precipitable water (mm)	**17.7**	**23.1**
Surface temperature (°C)	28.2	26.1
Surface dewpoint (°C)	*4.5*	*7.2*
700-hPa RH (%)	**42**	**56**
500-hPa RH (%)	58	65
800–500-hPa lapse rate (°C km^{-1})	**8.5**	**7.4**
Surface–500-hPa zonal shear (m s^{-1})	**9.9**	**2.3**
Depth of cloud base to −38°C level (m)	*5210*	*6036*

cloud base to the homogeneous freezing level, taken to be −38°C assuming ammonium sulfate cloud condensation nuclei (CCN) (DeMott et al. 1994), was calculated for both cases, and cloud depths are significantly larger in the nonreflective case. The explanation behind choosing the depth from the LCL to −38°C is found in section 5.

5. Cloud droplet residence time

If a large number of small ice crystals is indeed the source of ice clouds with enhanced 3.9-μm reflectivity, the next logical question becomes, Why do some thunderstorm tops have smaller ice crystals than others? Results from section 4 show that in the high plains during the summer months, certain thermodynamic environments favor thunderstorms with smaller ice crystals, but this offers little evidence into the physical mechanism leading to small ice production. Rosenfeld and Lensky (1998) discuss differences between microphysical profiles in maritime and continental clouds. Continental clouds have a deeper diffusional droplet growth zone than maritime clouds, so that continental cloud droplets forming near cloud base grow very slowly with depth as they ascend within the updraft. This effect is exaggerated as updraft magnitudes increase. Collision–coalescence efficiency decreases as cloud droplet size decreases, so these droplets remain relatively small even at temperatures well below freezing. Heymsfield et al. (2005) use aircraft measurements during CRYSTAL-FACE along with a 1D parcel model to study the effects of homogeneous ice nucleation in clouds with varying properties, including depth and updraft velocity. Their Figs. 13 and 16 show that stronger updrafts support larger supersaturation with respect to liquid

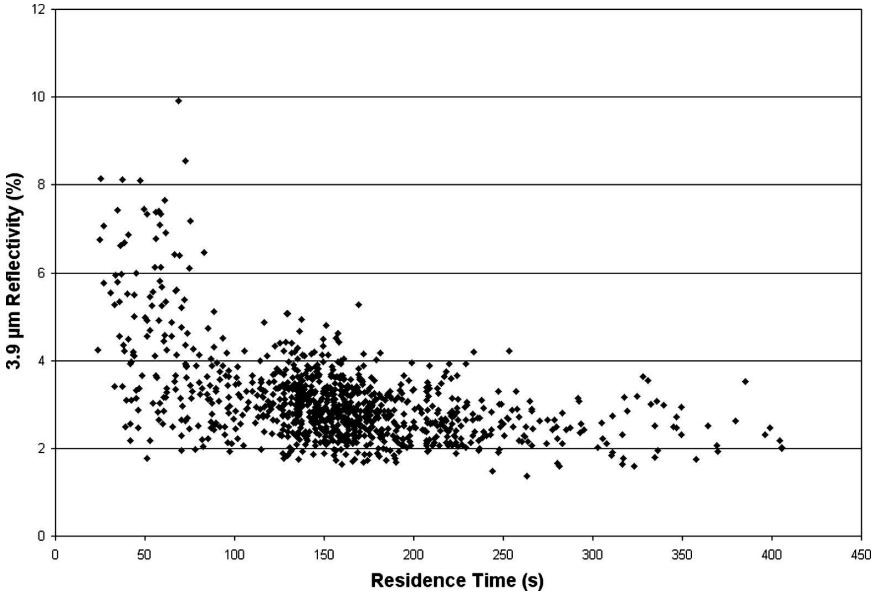

FIG. 7. Mean 3.9-μm reflectivity plotted against cloud droplet residence time (s) between the lifted condensation level and the −38°C level. This quantity is estimated by dividing the cloud depth by the square root of twice the CAPE.

water, which prevents the smallest droplets from evaporating before freezing homogeneously. Additionally, parcels initiated at colder temperatures produce smaller droplets and therefore smaller ice crystals. Their Fig. 14 shows that clouds whose cloud-base temperature is warmer (lower in altitude) produce significantly larger mean droplet diameters just prior to the onset of homogeneous ice nucleation, because droplets have a longer time to grow. These two studies suggest that, in general, the anvils of high-based clouds with strong updrafts contain smaller and more numerous ice crystals.

To test this hypothesis with satellite and NARR data, GOES-East data over all of the eastern United States from 2145 UTC on each of the 32 days described in section 4 (during the summer) were analyzed to select 978 individual clouds having at least 50 pixels with 10.7-μm brightness temperatures colder than −40°C. Images from 2145 UTC are used instead of those from 2345 UTC to maximize the available area with solar zenith angles less than 68°. For each cloud, the mean 3.9-μm reflectivity was calculated, and the nearest NARR grid point from 2100 UTC was selected. To eliminate nonconvective environments in the NARR data, only grid points whose mean-layer CAPE exceeded 200 J kg^{-1} and whose cloud depth between the LCL and the −38°C level exceeded 1 km were allowed. Since

$$w_{\max} = \sqrt{2 \times \text{CAPE}}, \tag{5}$$

where $w_{\max}$ is the maximum possible vertical velocity, we define a quantity called the cloud droplet residence time (τ) as

$$\tau = \frac{D_{\text{LCL}/-38}}{w_{\max}}, \tag{6}$$

where $D_{\text{LCL}/-38}$ is the depth from the LCL to the −38°C level. The cloud droplet residence time is a rough estimate of how long a cloud droplet that formed at cloud base exists within the updraft before reaching the −38°C level and is, therefore, a function of both cloud depth and updraft velocity. Figure 7 shows the mean 3.9-μm reflectivity of each cloud plotted against the NARR-derived residence time. Those 3.9-μm reflectivity values exceeding 5% were limited almost entirely to droplet residence times of less than 100 s; in other words, if a cloud droplet population remains below the homogeneous freezing level too long, its mean diameter will increase and its number concentration will decrease sufficiently to prevent significant reflection of incoming 3.9-μm radiation. The variance about a best-fit curve through the points in Fig. 7 could be explained by any of the following: 1) additional mechanisms, such as entrainment and CCN distributions, may play a role in anvil ice crystal properties; 2) errors in the NARR dataset, especially with the CAPE and surface temperature and moisture values matching the true environment in which each cloud forms; 3) 3.9-μm reflectivity is a function of more than just ice crystal mean

diameter; and 4) the GOES footprint is large, so 3.9-μm reflectivity measurements may not properly represent the actual cloud properties.

If the variance in Fig. 7 is dominated by errors in CAPE, one could theoretically measure the 3.9-μm reflectivity of a glaciated cloud, use nearby surface and sounding data to estimate the residence time, then compare the observed reflectivity value to the predicted value from a best-fit curve from Fig. 7. Observed reflectivities larger than the predicted value suggest that the sounding-observed CAPE is too low, and the actual updraft within the cloud is stronger than expected. In this way, 3.9-μm reflectivity may be used as a thunderstorm nowcasting tool to infer updraft strength. Further research is required to determine whether this method is practical. This physical mechanism is consistent with the climatological results in Figs. 2 and 4. Thunderstorms forming in the mountains and high plains tend to have relatively high bases, due to dry boundary layers and elevated terrain. The largest 3.9-μm reflectivity values in Figs. 2 and 4 occur just east of the Rocky Mountains, a region that will have both high cloud bases and fairly strong updrafts.

6. Concluding remarks

This study examines the reflectivity of thunderstorm tops as measured by the GOES 3.9-μm reflectivity product. A climatological analysis reveals that environmental conditions in mountainous regions of the United States favor storms with enhanced 3.9-μm reflectivity, while storm-top reflectivity over much of the eastern United States is lower. Model results suggest that these storm-top 3.9-μm reflectivity differences are due to variations in ice crystal size and number concentration; smaller ice crystal distribution mean diameters result in larger 3.9-μm reflectivities. Reanalysis data are used to show that highly reflective thunderstorms tend to occur in environments with relatively dry boundary layers, steep lapse rates, large vertical shear, and small distances from cloud base to the homogeneous freezing level. A physical mechanism, called the cloud droplet residence time, is presented, which explains why storms in mountainous areas have larger mean 3.9-μm reflectivities. If proven to be valid, thunderstorm updraft strength information can be obtained from GOES 3.9-μm reflectivity measurements. In addition, if a thunderstorm with fairly uniform 3.9-μm reflectivity values suddenly begins ejecting smaller ice crystals from its updraft, results of this study suggest that its updraft may have recently strengthened, allowing more tiny cloud droplets to freeze homogeneously. This observation potentially has extremely useful nowcasting applications.

Work is currently under way to improve the model simulations presented in section 3. We plan to use more sophisticated ways of representing the scattering phase function, along with allowing ice crystal habit to vary. The eventual goal is to obtain an accurate relationship between 3.9-μm reflectivity and ice crystal size and habit, so that satellite measurements of 3.9-μm reflectivity may provide information about the cloud-top microphysical structure. In addition, satellite measurements from other platforms, such as the Moderate Resolution Imaging Spectroradiometer instrument aboard the polar-orbiting satellites *Terra* and *Aqua* may provide independent estimates of ice crystal size to validate our model simulations.

Acknowledgments. This research was supported by NOAA Grant NA17RJ1228. The authors thank Drs. Mark DeMaria, Daniel Rosenfeld, and Andy Heymsfield for invaluable comments and discussion. Thanks also to Cindy Combs for the use of CIRA's cloud climatology, as well as John Weaver and Bob Rabin for excellent ideas and comments, and the National Climatic Data Center for the use of the NARR data. Finally, thanks to three anonymous reviewers for very insightful suggestions and comments. The views, opinions, and findings in this report are those of the authors, and should not be construed as an official NOAA and or U.S. government position, policy, or decision.

REFERENCES

Allen, R. C., Jr., P. A. Durkee, and C. H. Wash, 1990: Snow/cloud discrimination with multispectral satellite measurements. *J. Appl. Meteor.,* **29,** 994–1004.

DeMott, P. J., M. P. Myers, and W. Cotton, 1994: Parameterizations and impact of ice initiation processes relevant to numerical model simulations of cirrus clouds. *J. Atmos. Sci.,* **51,** 77–90.

Ellrod, G. P., 1995: Advances in the detection and analysis of fog at night using GOES multispectral infrared imagery. *Wea. Forecasting,* **10,** 606–619.

Grasso, L. D., and T. J. Greenwald, 2004: Analysis of 10.7-μm brightness temperatures of a simulated thunderstorm with two-moment microphysics. *Mon. Wea. Rev.,* **132,** 815–825.

Greenwald, T. J., R. Hertenstein, and T. Vukićević, 2002: An all-weather observational operator for radiance data assimilation with mesoscale forecast models. *Mon. Wea. Rev.,* **130,** 1882–1897.

Heymsfield, A. J., L. M. Miloshevich, C. Schmitt, A. Bansemer, C. Twohy, M. R. Poellot, A. Fridlind, and H. Gerber, 2005: Homogeneous ice nucleation in subtropical and tropical convection and its influence on cirrus anvil microphysics. *J. Atmos. Sci.,* **62,** 41–64.

Kidder, S. Q., and T. H. Vonder Haar, 1995: *Satellite Meteorology: An Introduction.* Academic Press, 466 pp.

——, D. W. Hillger, A. J. Mostek, and K. J. Schrab, 2000: Two simple GOES imager products for improved weather analysis and forecasting. *Natl. Wea. Dig.,* **24** (4), 25–30.

Liljas, E., 1987: Multispectral methods for cloud classification. *Proc. Satellite and Radar Imagery Interpretation Workshop,* Reading, United Kingdom, European Organization for the Exploitation of Meteorological Satellites, 475–493.

Melani, S., E. Cattani, V. Levizzani, M. Cervino, and F. Torricella, 2003a: Radiative effects of simulated cirrus clouds on top of a deep convective storm in METEOSAT second generation SEVIRI channels. *Meteor. Atmos. Phys.,* **83,** 109–122.

——, ——, F. Torricella, and V. Levizzani, 2003b: Characterization of plumes on top of a deep convective storm using AVHRR imagery and radiative transfer model simulations. *Atmos. Res.,* **67–68,** 485–499.

Mesinger, F., and Coauthors, 2006: North American regional reanalysis. *Bull. Amer. Meteor. Soc.,* **87,** 343–360.

Mitchell, D. L., 1996: Use of mass- and area-dimensional power laws for determining precipitation particle terminal velocities. *J. Atmos. Sci.,* **53,** 1710–1723.

——, 2000: Parameterization of the Mie extinction and absorption coefficients for water clouds. *J. Atmos. Sci.,* **57,** 1311–1326.

Rosenfeld, D., and I. M. Lensky, 1998: Satellite-based insights into precipitation formation processes in continental and maritime convective clouds. *Bull. Amer. Meteor. Soc.,* **79,** 2457–2476.

Scorer, R. S., 1987: Convective rain as seen by channel 3. *Proc. Satellite and Radar Imagery Interpretation Workshop,* Reading, United Kingdom, European Organization for the Exploitation of Meteorological Satellites, 509–513.

Setvák, M., and C. A. Doswell III, 1991: The AVHRR channel 3 cloud top reflectivity of convective storms. *Mon. Wea. Rev.,* **119,** 841–847.

——, R. M. Rabin, C. A. Doswell III, and V. Levizzani, 2003: Satellite observations of convective storm tops in the 1.6, 3.7, and 3.9 μm spectral bands. *Atmos. Res.,* **66–67,** 607–627.

Stephens, G. L., 1978: Radiation profiles in extended water clouds. Part II: Parameterization schemes. *J. Atmos. Sci.,* **35,** 2123–2132.

Turk, J., J. Vivekanandan, T. Lee, P. Durkee, and K. Nielsen, 1998: Derivation and applications of near-infrared cloud reflectances from *GOES-8* and *GOES-9. J. Appl. Meteor.,* **37,** 819–831.